Miao, X., Zhang, Q., Wang, L., Jiang, H. & Qi, H. (2015). Application of riblets on turbine blade endwall secondary flow control. Journal of Propulsion and Power, 31(6), pp. 1578-1585. doi: 10.2514/1.B35549

CITY UNIVERSITY LONDON

EST 1894

City Research Online

Original citation: Miao, X., Zhang, Q., Wang, L., Jiang, H. & Qi, H. (2015). Application of riblets on turbine blade endwall secondary flow control. Journal of Propulsion and Power, 31(6), pp. 1578-1585. doi: 10.2514/1.B35549

Permanent City Research Online URL: http://openaccess.city.ac.uk/13184/

Application of Riblets on Turbine Blade End-wall Secondary Flow Control

X. Miao[1], Q. Zhang[1,2],L.Wang[1], H. Jiang[1], and H. Qi[1]

Within the past ten years, significant improvements have been achieved in the laser manufacturing process. It is feasible now to design various small-scale surface features (such as dimples, riblets, grooves, etc.) in gas turbine applications with the current manufacturing readiness level of laser surface texturing techniques. In this paper, the potential of adding riblets on turbine end-wall has been investigated through combined CFD and experimental studies in a low speed linear cascade environment. Detailed comparisons of the flow structures have been made for cases with and without riblets on the end-wall. The numerical results show that end-wall riblets can effectively reduce the strength of the pressure side leg of the horseshoe vortex, lower the cross passage pressure gradient, and alleviate the lift up of the passage vortex. Oil film flow visualization and exit aerodynamic loss survey in experiments support the CFD observations: the passage vortex loss core moves closer to the end-wall with the addition of riblets. The present study consistently demonstrates that the addition of riblets can be an effective approach to reduce the end-wall secondary flow. Further research questions are raised for the applicability of riblets concept in actual engine conditions and options for design optimization.

Nomenclature

C = Chord or Probe calibration coefficient

C_p = Pressure loss coefficient $C_p = \frac{P_{01} - P_0}{\frac{1}{2}\rho v^2}$

[1]University of Michigan-Shanghai Jiao Tong University Joint Institute, Shanghai, China.
[2] School of Engineering and Mathematical Sciences, City University London, London, UK.
 (Corresponding author: Qiang.Zhang@city.ac.uk)

C_x	=	Axial chord
DOE	=	Design of Experiments
LDV	=	Laser Doppler Velocimetry
LP	=	Low pressure
LPD	=	Laser powder deposition
P	=	Pressure or Blade Pitch
R/S	=	Radius-wise location normalized by blade span
S	=	Blade span
V	=	Velocity
y/P	=	Pitch-wise measurement location normalized by blade pitch
y+	=	Non-dimensional wall distance: $y^+ \equiv u_t\, y/\nu$
α	=	Probe calibration flow (pitch) angle
β	=	Probe calibration flow (yaw) angle
λ_2	=	the second eigenvalue of the second in variant of the velocity gradient tensor

Subscript

o	=	total
A	=	Three-hole probe center channel
avg	=	Average of A, B and C (three-hole channels)
B	=	Left-hole probe angled channel
C	=	Top-hole probe angled channel
D	=	Right-hole probe angled channel
T	=	Probe calibration total pressure
α	=	Probe calibration flow (pitch) angle
β	=	Probe calibration flow (yaw) angle
1	=	Blade row inlet, radial position

I. Introduction

A. End-wall Secondary Flow and Loss Reduction

Endwall secondary flow has been investigated for more than 50 years in the gas turbine community. The aerodynamics loss due to such secondary flow can be as high as 30%-50% of the total loss in a blade row (Sharma and Butler [1]). Substantial extra heat load would also be introduced by the end-wall vortical flow. A significant amount of efforts have been devoted in controlling the end-wall secondary flow.

Sieverding [2] and Langston [3] reviewed the main work in the secondary flow physics and theories. Hawthorne [4] first described the classic end-wall vortex system. After his work, many researchers found the evidences of secondary flow and horseshoe vortex in turbine passage. Langston et al. [5] presented a secondary flow model based on their measurements: the fluids within the inlet boundary layer separate at the saddle point and form the horseshoe vortex. One leg of the horseshoe vortex is drawn into the passage towards the suction side and becomes the passage vortex by the cross pressure gradient, the other leg is drawn into the adjacent passage and becomes a counter vortex. It needs to be pointed out that there are some different secondary flow models, whose strength, stability, and detailed structures are largely dependent upon the blade loading, flow turning angle, Reynolds numbers, Mach numbers, etc. Sieverding and Bosche [6] showed the development and interaction of the passage vortex and counter vortex by using colored smoke wire technique. In their experiments, the pressure leg and suction leg of horseshoe vortex were clearly distinguished by different smoke colors. They concluded that the horseshoe vortex and passage vortex do not exist independently, both of them are part of the same vortex structure. Flow visualization by Wang et al. [7] provided a more detailed insight into flow structures near the leading edge of their cascade. In practice, secondary flow loss can be effectively reduced by end-wall contouring, leading edge modifications, end-wall fence, cooling injection, etc.

End-wall contouring is a passive flow control method developed to reduce the strength of the passage vortex by varying the cross passage pressure gradient. In the early nineties, Rose [8]proposed that flat end-walls should no longer be a necessary design constraint and aerodynamic benefits could arise from profiling the end-walls. Convex curvature near the pressure surface and concave curvature near the suction side were applied to the end-wall in the early study of Yan et al. [9]. Their experimental and computational results proved that 3D end-wall contouring can reduce 20% of the pressure loss. Harvey et al. [10] and Hartland, et al. [11] reported a net total loss reduction of 20% and net secondary loss reduction of 30% by their end-wall modification for a large-scale, low-speed rotor in a

linear cascade. Ingram et al. [12] showed a 24% reduction in the secondary loss achieved by an optimal end-wall profile. Saha and Acharya [13] investigated 3D end-wall contouring with two combined curves varying in both streamwise and pitchwise directions. They found that, for the near wall region, the pitchwise pressure gradients are reduced, and the flow is more aligned with the midspan inviscid streamwise flow direction with a lower yaw angle. Praisner et al. [14] studied the application of non-axisymmetric end-wall contouring to mitigate the end-wall losses of LP turbine airfoil designs. In the study of Brennan et al. [15], the HP turbine of the Rolls-Royce Trent 500 engine was redesigned with the application of non-axisymmetric end-walls. Results showed that the addition of profiling to the end-walls reduces secondary loss by 0.24% of stage efficiency for the NGV and by 0.16% for the Rotor. The total efficiency for the HP Turbine is increased by 0.4%. Snedden et al. [16-17] studied the influence of a generic end wall design on the secondary flows structure. Their results indicated a 0.4% improvement in rotor efficiency. Recently, a new method for designing non-axisymmetric end-wall contours was proposed by Schobeiri and Lu [18]. By constructing the end-wall contour, the pressure difference on the hub can be controlled to reduce the secondary flow and increase the efficiency.

Leading edge modification is another common approach to vary the horseshoe vortex development. Sauer and Wolf [19] employed a bulb geometry on an inlet guide vane. They found the bulb geometry can increase the strength of counter vortex, which results in a reduction of passage vortex due to the counter-rotation of these two vortices. Zess and Thole [20] performed experimental and numerical investigations on leading edge fillet. Their results indicated that the fillet design can effectively accelerate the incoming boundary layer and reduce the turbulent kinetic energy and streamwise vortices levels, therefore reduce the strength of horseshoe vortex. Sauer bulb and a fillet geometry were investigated by Becz et al. [21]. Their results showed that both the small bulb and fillet geometries can reduce the area-averaged total loss by 8%.

The concept of end-wall fence is to stop the cross passage flow from pressure side to suction side by adding fence which height is larger than the inlet momentum thickness onto the end-wall. Chung et al. [22] used one streamwise fence to block and change the migration of the pressure side leg of the horseshoe vortex. Comparisons of the flow patterns obtained by flow visualization and LDV measurements showed that the fence is effective in reducing the highly skewed flow motion on the near end-wall suction side surface due to the passage vortex. Recently, Govardhan et al. [23] also proved that the fences are effective in weakening the end-wall cross flow.

However, due to the extensive cooling requirement for the fence to survive the high local heat load, the end-wall fence is almost impossible to be applied to the real turbine environment.

B. Manufacturability of Riblets

It is feasible now to design and apply small-scale engineered surface features in gas turbine environment. Within the past ten years, significant improvements have been achieved in the manufacturing process. Profile grinding and laser machining are commonly used processes for riblets manufacturing in industry [24-25]. Denkena et al. [25] demonstrated a method of manufacturing riblet structures directly onto extensive metal surface by profile grinding. The produced micro-scale riblets with the V-shaped cross-section profiles were tested in fluid dynamic experiments and are capable to reduce the skin friction by up to 4%. In Siegel's [26] study, micro-structuring surface of metal is produced using a picosecond pulsed laser ablation technique. A 7.2 % reduction in pressure loss has been achieved. However, the picosecond laser micro-machining has its limitations in achievable ablation rates, which could be improved by adapted system technology and optimized machining strategy.

To compromise between quality and efficiency, processes such as EDM [27], micro milling , micro planning [28] and micro grinding [29] can all be used to produce micro-level riblets with a minimum feature size around 20 μm. However, these processes have common limitations in riblet manufacturing as an industrial economical and effective way due to their relatively low material removal rates. The rolling process demonstrated by Hirt et al. [30] has a comparatively higher efficiency, however, the produced minimal structure dimension is above 100 μm.

The Laser Powder Deposition technique (LPD) has become an attractive process in aerospace manufacturing industry. In this process, a focused, intense source of laser energy was used to create a small molten pool (as small as 0.3 mm) with high absorptive efficiency. The heat-affected zone is typically much smaller than other processes. Fine metal powder was melted on the base material by scanning laser beam layer by layer [31]. This technique is well suited to the production of high-strength near net shaped components at low manufacturing volumes [32]. As such, it provides a more flexible and efficient way to manufacture thin-walled structures than the conventional manufacturing processes.

C. Motivation of the Pressure Study

The research idea of the present study is motivated by the current riblets manufacturing readiness level and its potential in end-wall secondary flow control. Unlike many other innovative designs which lack the

manufacturability, the end-wall riblets concept can be directly applied to the real turbine design if it can be proved to be effective in reducing the end-wall secondary flow.

Considering the complexity of secondary flow and various operating conditions in the real engines, the intention of this study is not to demonstrate a successful complete story about the end-wall riblets concept. Rather, it tries to open a new research option for end-wall secondary flow control on the basis of our wisdom gained in the past 50 years.

The work presented in this paper is a combined CFD and experimental study. For the purpose of aligning the end-wall fluid and blocking the cross passage flow migration, a series of small-scale riblets were added onto the end-wall region of a typical LP turbine blade, following the streamlines of the passage flow. Detailed comparisons of flow structures for numerical cases with and without end-wall riblets are introduced first. Oil film flow visualization and loss survey in a low speed linear cascade are shown next to validate the findings from the CFD study.

II.   Experimental Apparatus and Procedures

A. Test Section

A low speed wind tunnel was employed in the present study. A 25kw blower is connected with a large-sized flow stabilizer with flow straightener and meshes installed inside, which ensures the uniformity of the inlet flow. The stabilizer is then connected to a cascade test section, as shown in Fig. 1.
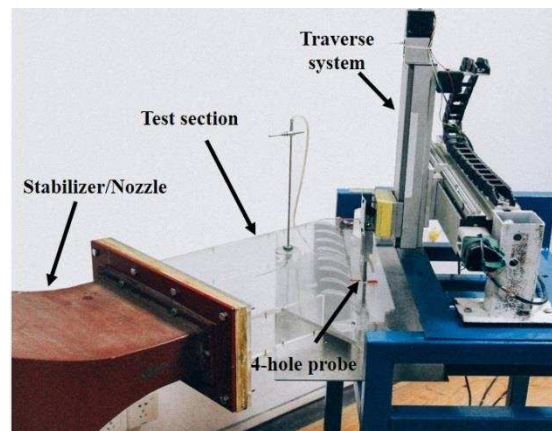

Fig. 1 Low speed wind tunnel and test section employed in the present study.

The test section consists of seven passages and eight blades. A schematic is shown in Fig. 2. There are two boundary-layer bleeds near the leading edge of the two side wall blades to help achieve a better flow periodicity.

Two movable tailboards are also attached at the exit section. The flow periodicity was verified by a full traverse of pressure measurement in the mid-span of the test section exit. A 2D traverse system was used to drive a four-hole probe for detailed aerodynamic loss measurements. The traverse measurement plane is located at 0.2 axial chord downstream of the blade trailing edge. Inlet stagnation and static pressure were measured by using a pitot-static probe located 1.5 axial chord upstream of the test blade leading edge. The turbulence level of the inlet flow is around 1%.

<div align="center">(a)   (b)</div>
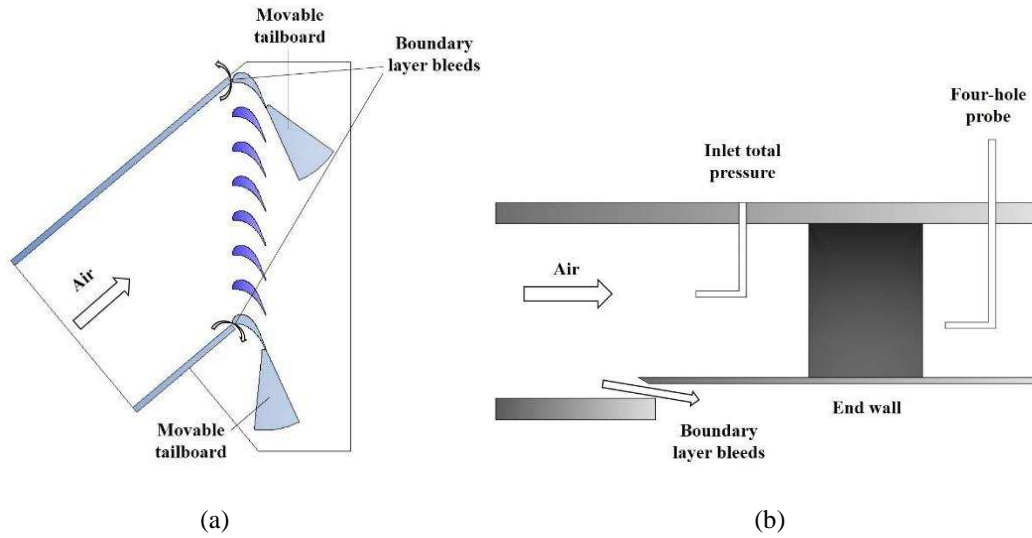
<div align="center">Fig.2 A schematic of the test section: (a) Top view (b) Side view.</div>

A boundary layer trip was placed 10mm after the end-wall boundary bleeds, which is located at 1.8 axial chord upstream of the test blade leading edge. The incoming end-wall boundary layer survey was conducted by using a boundary layer probe (flattened tip, sensing head diameter 0.3mm) located 1.5 axial chord upstream of the leading edge and 3 pitch to the upper movable tailboard. The measured velocity profiles were set as the inlet boundary condition in the CFD study.

A typical LP turbine blade design was adopted in the present study. The blade profile is similar to the one employed by Harrison [33] and Denton [34]. Detailed information of flow conditions and the blade design is shown in Table 1.

Table 1 Detailed flow condition and blade geometries	
Inlet Reynolds number (based on Cx)	3.77×10^4
Exit Reynolds Number (based on C_x)	7.64×10^4
Mass flow rate (full passage)	0.31 kg/s
True chord	67.6mm
Axial chord	54mm
Pitch	56mm
Span	73mm
Inlet blade/flow angle (from axial)	40°
Mean exit flow angle (from axial)	65.5°
Inlet momentum thickness	0.6mm
Inlet displacement thickness	0.67mm

B. Four-hole Probe Measurement and Calibration

An L-shape four-hole probe was employed in the experimental study. The probe was constructed from four stainless steel tubes of 1.0mm outer diameter and 0.4mm inner diameter, giving an overall tip outer diameter of 3.0mm. The three outer tubes are evenly located around the center tube and each of them has a 60° face angle. The probe was calibrated in the present low speed wind tunnel (with a same Reynolds number range as the loss survey). In the calibration process, the pitch (α) and yaw (β) flow angle ranges are, $-20° \leqslant \alpha \leqslant 20°$ and $-16° \leqslant \beta \leqslant 16°$. Fig.3 shows the four-hole probe employed and two calibration maps, including a total pressure calibration matrix $C_T (\alpha, \beta)$ and an application matrix $C_T (C_\alpha, C_\beta,)$. The detailed computation technique is described by Main et al. [35]. The coefficients C_α, C_β and C_T are defined as follows,

$$C_\alpha = \frac{P_B - \frac{1}{2}(P_C + P_D)}{P_A - P_{avg}} \qquad (1)$$

$$C_\beta = \frac{P_C - P_D}{P_A - P_{avg}} \qquad (2)$$

$$C_T = \frac{P_0 - P_A}{P_A - P_{avg}} \qquad (3)$$

$$P_{avg} = \frac{P_B + P_C + P_D}{3} \qquad (4)$$

The calibration map is largely symmetric, as shown in Fig. 3. Other calibration maps for C_α and C_β, also indicate a good performance of the probe. With this calibration data, the total pressure and flow angles can be obtained by linear interpolation and lookup of the application matrix.
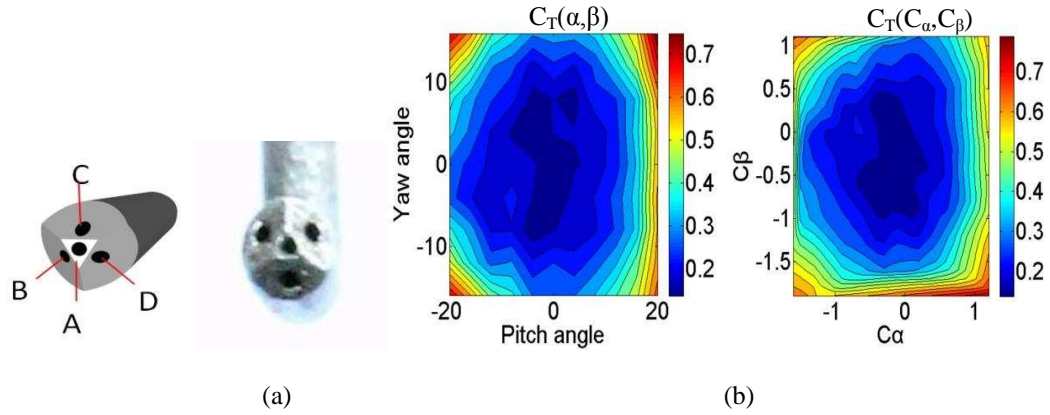
Fig.3 (a) Four-hole probe and (b) calibration maps.

During the exit total pressure loss survey, pressure measurements were taken at fifteen pitch-wise locations and ten span-wise locations for the lower half blade span. At each traverse location, pressure data were taken for 10 seconds at a sampling rate of 1k.

Sensor Techniques HCLA pressure sensors were used for pressure measurements. These sensors were calibrated with a Beamex MC2-MF multifunction calibrator (accuracy 0.05% FS). During the measurements, all differential pressure sensors were referenced with the inlet total pressure to reduce the correlated bias error.

The experimental uncertainty for loss coefficient Cp is 0.0135 for a typical nominal value of 0.3 (95% confidence level).

C. Flow Visualization by Oil Film Method

In the present study, flow visualization was carried out by an oil film method described in Lee et al. [36]. A general procedure is briefly introduced here. Prior to each wind tunnel test, a mixture of black carbon powder and kerosene was evenly spread on the passage end-wall. A white adhesive contact paper (0.1mm in thickness) was attached to the lower half-span of the suction side surface to distinguish the oil film from the blade background. With the flow passing the blade passage, the oil film gradually developed along the end-wall and the suction side surface. After the complete evaporation of kerosene, the final impingement path of passage vortex can then be clearly identified on the white contact paper. A high resolution digital camera was used to capture the surface flow traces in this oil film experiment.

9

D. Riblets fabrication: Laser Powder Deposition technique (LPD)

The Laser Powder Deposition technique (LPD) was used to fabricate the small-scale riblets employed in the present study. Figure 4 shows a sample of the riblets fabricated on a steel plate by the LPD technique. The relative locations and detailed dimensions of the riblets are also shown in Fig. 4.

The experimental setup for the deposition consists of a continuous wave Ytterbium fiber laser (YLS-1000-CT) with a wavelength of 1080nm, a max laser with a power output of 1000w, and a Staubli TX90 robot with CS8 controller. The powder used is Inconel 718 in the size range of 45-105 µm, delivered through a coaxial nozzle along with argon gas. To achieve reliability and consistency of thin wall manufacturing, Design of Experiments (DOE) approach was adopted. A 0.9mm thick, 0.9mm high riblet was finally built with a laser power of 120w, scanning speed of 4mm/s, and powder feed rate of 3g/min.
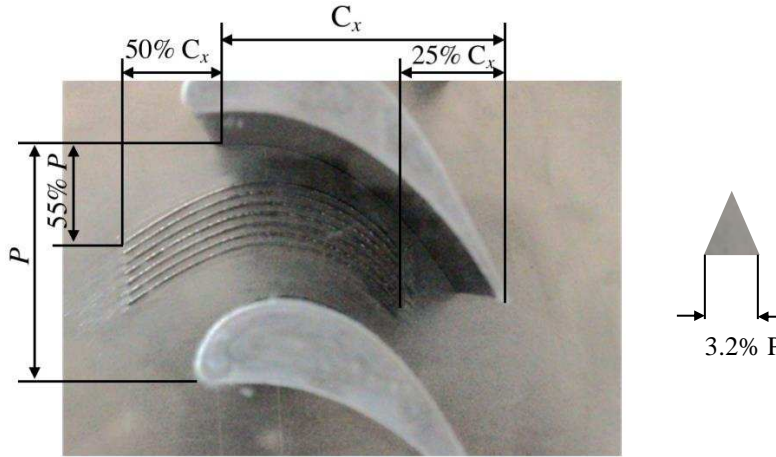

Fig 4. Deposited riblets on end-wall by using LPD technique

III.   Computational Approach and Details

ANSYS FLUENT 14.5 was employed in the present numerical study. This commercial CFD solver solves the three-dimensional, steady, turbulent form of the Reynolds-Averaged Navier-Stokes (RANS) equations with a finite volume method. Fig.6 shows the computational domain which consists of one blade with periodic boundary conditions. The blade definition, flow angle, and inlet boundary conditions are the same as the experimental arrangement.

The k-ω SST turbulence model was chosen in the present study. No further efforts have been made to evaluate different RANS turbulence models. It was assumed that, with consistent boundary conditions and meshing scheme,

the k-ω SST turbulence model should be capable of ranking the qualitative differences in flow physics made by end-wall riblets.

A commercial meshing tool, Pointwise, was used for mesh generation. Figure 5 also shows the fully structured hexahedra mesh employed in the present study. The near end-wall riblets mesh resolution varies to check the final solutions' grid independency. An enlarged view of three mesh resolutions near riblets region is shown in Fig. 5. For all grid levels, the near end-wall y+ value is around 1. Note that the same mesh distribution was also implemented for the case without riblets to minimize the grid effect.

Flow visualization of the solutions was performed using the Ensight software.
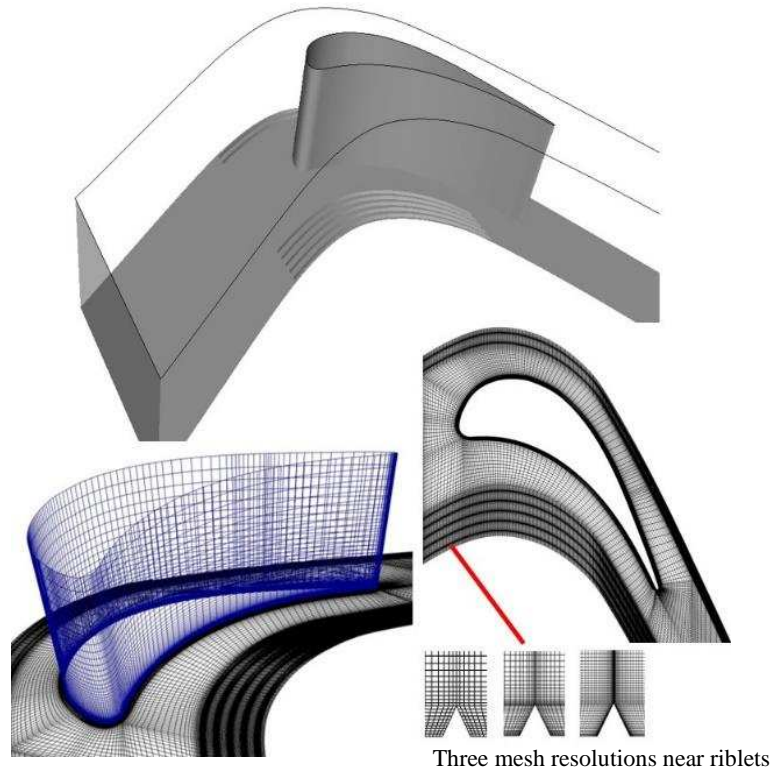

Three mesh resolutions near riblets

Fig. 5 Computational domain and mesh

Figure 6 shows both spanwise and pitchwise-averaged loss coefficient Cp obtained with three density levels of grids at 0.2 chord downstream of the cascade blade. Negligible difference between results from 7 million and 9 million grids observed. In the present study, 7.1 million and 7 million grids were used for calculations with and without riblets, respectively.
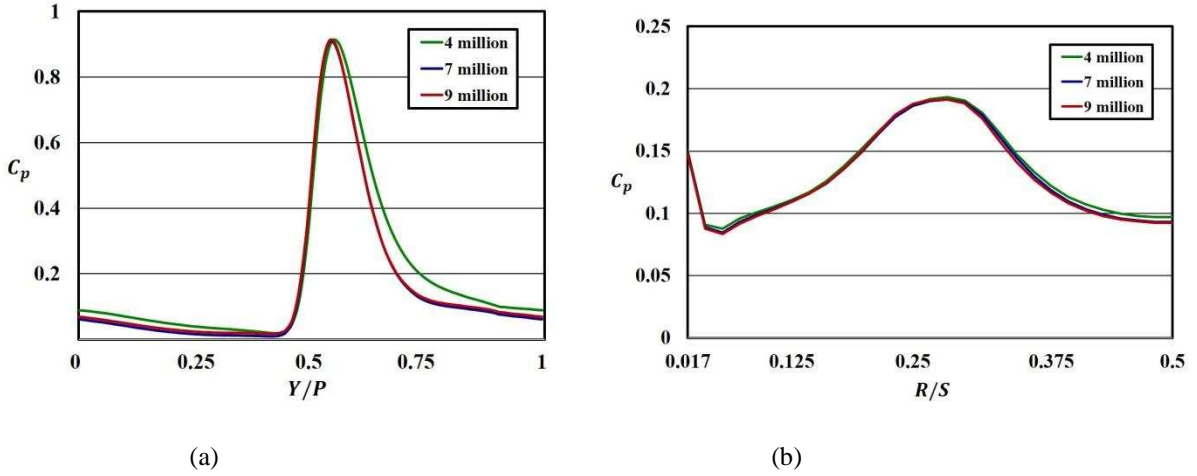
Fig. 6 Grid independence study: (a) span-wise and (b) Pitchwise averaged loss coefficient Cp at 0.2 chord downstream of the cascade blade, obtained with three density levels of grids.

IV.   Results and Discussions

This section firstly presents CFD results to demonstrate the influence of end-wall riblets on the end-wall secondary flow structure. Experimental data of exit loss survey and images obtained by oil film method are presented next to validate and compare with the CFD results.

A. Secondary Flow Structure with Riblets (CFD)

Firstly, vorticity contours along three passage cut planes are shown in Fig. 7a for the case without riblets. The pressure side horseshoe vortex core is illustrated by a blue streamline (released from the inlet boundary layer) which separates at a saddle point near the blade leading edge, rolls towards the suction side surface, and merges into the passage vortex. The suction side horseshoe vortex leg ("counter vortex") is illustrated by a streamline colored in red. Figure 7b presents the differences in flow structure made by the end-wall riblets: (1) the strength of the pressure side leg of the horseshoe vortex is greatly reduced through the passage (lower vorticity); (2) the passage vortex developed downstream is confined closer to the end-wall while migrating towards the suction side; (3) discrete high-vorticity regions near the end-wall indicate the existence of small-scale vortices between riblets.
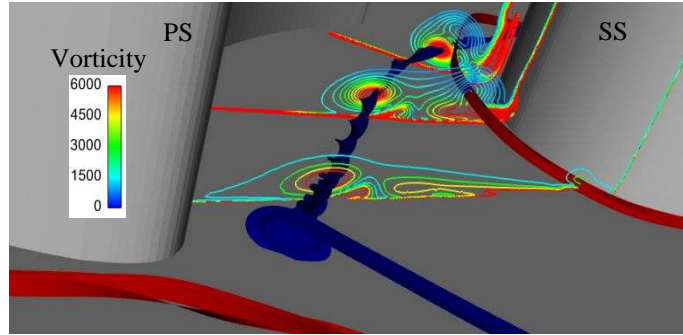
(a)
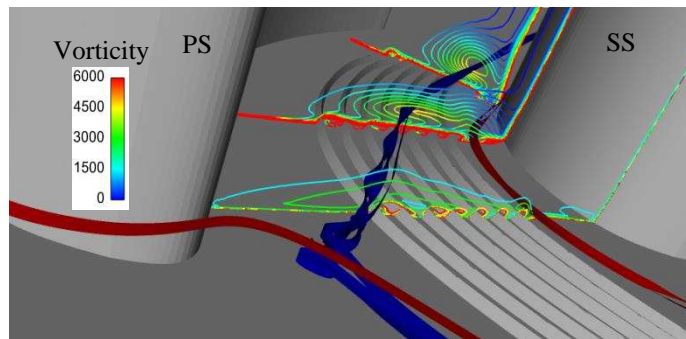
(b)

Fig. 7Iso-vorticity contours along three cut planes in the passage for cases (a) without and (b) with riblets (CFD).

Figure 8 presents an end-wall top view, illustrating the development of end-wall streamlines with and without riblets. It can be clearly observed that the early over-turning of some near wall fluids is effectively reduced by the riblets structure. The near wall flow becomes more aligned with the streamline curvature of the end-wall riblets.
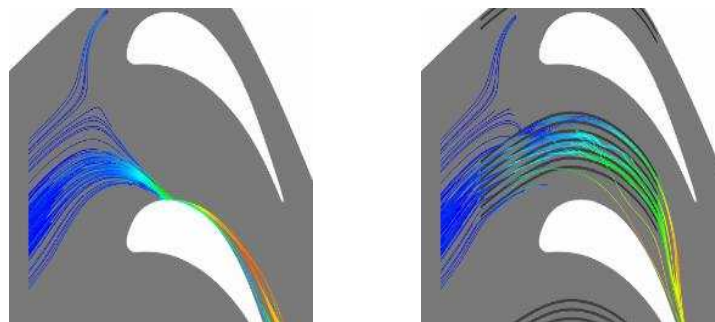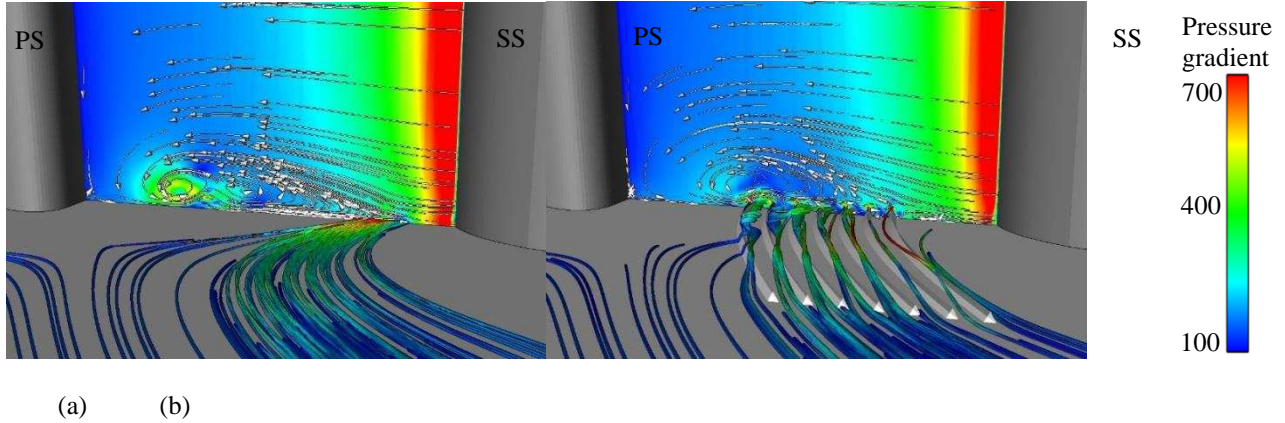

(a)   (b)

Fig. 8 Fluid streamlines near the end-wallfor cases (a) without and (b) with riblets (CFD).

Pressure gradient contours and streamlines near the passage leading edge region are further illustrated in Fig. 9. Secondary flow velocity vectors are also plotted on the same cut plane. Local pressure gradient near the end-wall is

13

greatly lowered by the addition of riblets. The rolling and early development of end-wall passage vortex are held up in this region, as shown by the secondary flow vector and the near wall streamlines. Near the end-wall riblets region, the streamlines indicate that some small-scale vortices develop and roll in the small channels between riblets.

(a)   (b)

Fig. 9 Pressure gradient contours and streamlines near the passage leading edge for cases (a) without and (b) with riblets (CFD).

Figure 10 presents the passage flow vortical structure visualized based on iso-surfaces of λ_2 [37, 38]. Same negative λ_2 value was selected for better illustration for both cases with and without riblets. For the case without riblets, the passage vortex is lifted up from the end-wall, and a passage vortex loss core is formed next to the wake region, shown by the loss coefficient Cp contour in Fig. 10a. With the addition of riblets, the passage vortex stays at a much lower position near the exit of the blade passage, as shown in Fig. 10b.
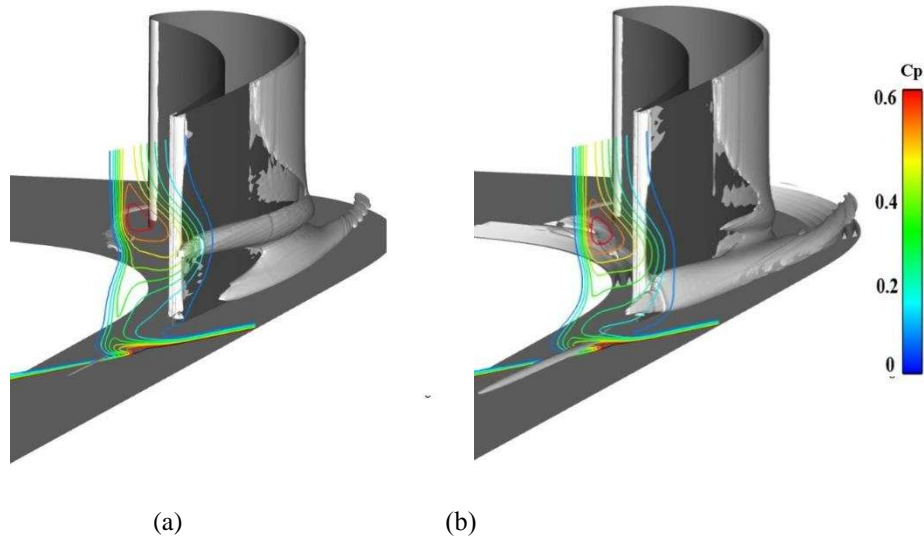
(a)   (b)

Fig. 10 Loss coefficient contour and iso-surfaces of λ_2 for cases (a) without and (b) with riblets (CFD).

14

B. Experimental Result

Flow traces on the suction side surface (near end-wall region) are visualized with an oil film method in the present experimental study. Figure 11 shows two images obtained for conditions with and without riblets on the end-wall. Clearly, the oil film develops to a much lower level on the suction side surface for the case with riblets. This observation is consistent with the flow structure from CFD result as illustrated in Fig. 10.

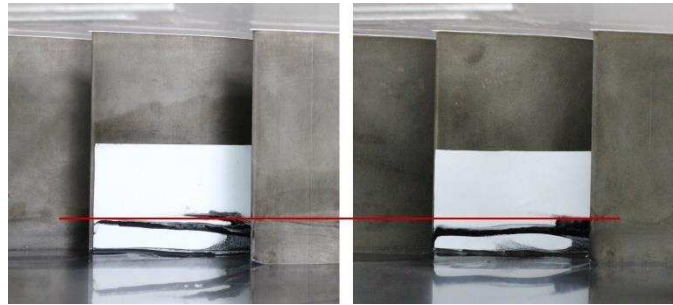(a)   (b)

Fig. 11 Flow traces for cases (a) without and (b) with riblets on the suction side surface (near end-wall) obtained by oil film experiment.

Figure 12 presents experimental result of loss coefficient Cp distributions for conditions with and without riblets. These data were obtained at 0.2 chord downstream of the blade through the 4-hole probe survey. Note that no attempt was made to measure pressure data within 1.5 mm height to the end-wall due to concerns with the probe-wall interaction. The profile loss for near mid-span region is very similar for both cases. The circled regions in Fig. 12a and 12b are identified as the passage vortex signatures in the wake. For the case with riblets, a higher loss region is drawn closer to the end-wall.
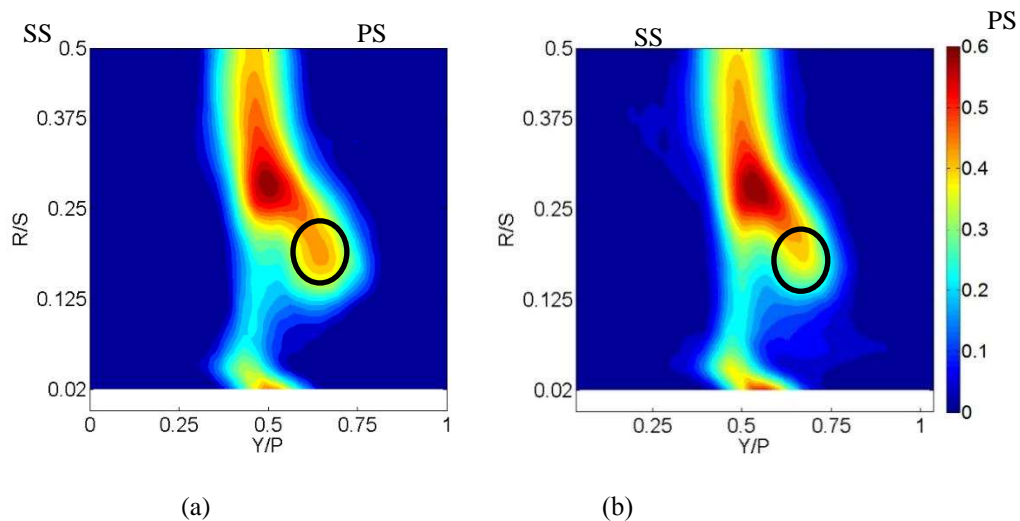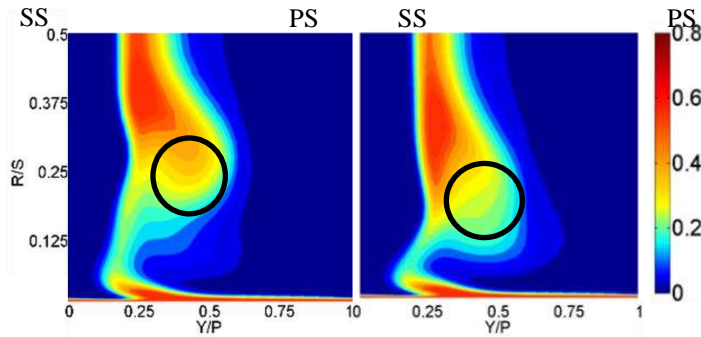

(a)   (b)

Fig. 12 Aerodynamic loss coefficient Cp distributions for cases (a) without and (b) with riblets obtained 0.2 chord downstream of the cascade blade.(Experimental study)

15

(a)   (b)

Fig. 13 Aerodynamic loss coefficient Cp distributions for cases (a) without and (b) with riblets obtained 0.2 chord downstream of the cascade blade.(CFD)

Fig. 13 shows results of loss coefficient Cp distributions obtained by CFD simulations, conducted with same boundary conditions as the experimental study. For the case without end-wall riblets, the passage vortex loss core can be clearly identified above the end-wall, as shown in Fig. 13a (circled next to the wake). With end-wall riblets, the loss core location is varied significantly. Fig. 13b shows a similar pattern as the experimental contour data in Fig. 12b (as well as CFD result in Fig. 10b).

Quantitatively, there are some expected discrepancies between CFD and experimental results. In general, less diffusion can be observed from the CFD loss contours. Note that the surface finish of the riblets fabricated with LPD technique is not perfectly smooth. All blade surface roughness level has not been measured and taken into account in the CFD simulation.

Qualitatively, both CFD and experimental results show a consistent trend: the passage vortex loss core is drawn closer to the end-wall with the addition of riblets.

C. Overall Aerodynamic Loss and Optimization Strategies

It has been found that the riblets design has to be further optimized to gain desired overall aerodynamic benefit. Observed from experiments and numerical results in the present study, the differences of overall mass-averaged aerodynamic loss coefficient with and without adding riblets are less than one percent, which are within uncertainties in experiments and RANS CFD.

It has been recognized that additional loss penalty can also be introduced by the riblets surface roughness (un-characterized in the experiments). Friction and the mixing loss from the small-scale vortices near riblets (shown in Fig. 8 and 10) will accumulate and be convected downstream through the passage. The beneficial effect of

secondary flow control needs to overcome these unavoidable side effects. Dirt and fouling in engine operating condition could also alter the performance of endwall riblets, which should be further evaluated.

The riblets geometry optimization should be conducted by a thorough parametric study (beyond the scope of the present paper). Strategy-wise, the detailed geometry has to be determined according to the incoming flow boundary layer thickness, the passage turbulence level, Reynolds number, blade loading, etc. Uniform riblets height is not necessary since the need for local flow alignment varies in pitch-wise and axial-wise.

Additional impact from riblets on the heat load reduction also needs to be noted: the reduction of passage vortex size and strength will significantly reduce the heat load near the blade suction surface, and thus lower the local cooling requirement on the blade. In the overall budget, this beneficial effect has to be balanced with the negative effects of increased vorticity between riblets and surface area on end-wall heat transfer.

V. Summary and Conclusion

Incented by the manufacturability of riblets in gas turbine industry, the present work exploited the potential of controlling the end-wall secondary flow with riblets through a combined experimental and CFD study.

The numerical predictions were undertaken using the FLUENT with the SST k-ω turbulence model. Detailed comparisons of the passage flow structures were made in CFD simulations for cases with and without end-wall riblets. These comparisons suggest that the end-wall riblets greatly reduce the strength of the pressure side leg of the horseshoe vortex, lower the cross passage pressure gradient, and alleviate the lift up of the passage vortex.

Oil film flow visualization and exit aerodynamic loss survey were conducted in a low speed linear cascade experimental facility. Laser Powder Deposition technique (LPD) was used to manufacture the small-scale riblets. Qualitatively all experimental data support the CFD observations: the passage vortex loss core moves closer to the end-wall with the addition of riblets.

The new end-wall riblets concept proposed in this study provides a new research option to control the end-wall secondary flow. However, it should be noted that, in an actual engine, the high turbulence level and unsteady flow with wakes from upstream blade rows could also affect the performance of riblets. Further investigations are needed to optimize the riblets design and evaluate its applicability in these different flow conditions.

Acknowledgments

References

[1] Sharma, O., and Butler, T., 1987, "Predictions of End-wall Losses and Secondary Flows in Axial Flow Turbine Cascades," ASME J. Turbomach., 109, pp. 229-236.

[2] Sieverding, C., 1985, "Recent progress in the understanding of basic aspects of secondary flows in turbine blades passages," ASME J. Engineering for Gas Turbines and Power, 107(2), pp. 248-257.

[3] Langston, L. S., 2001, "Secondary flows in axial turbines-a review," Ann. N.Y. Acad. Sci., 934(1), pp. 11-26.

[4] Hawthorne, W. R., 1955, "Rotatiional Flow through Cascades," The Quarterly Journal of Mechanics and Applied Mathemati, 8(3), 266-292.

[5] Langston, L. S., 1980, "Cross flows in a Turbine Cascade Passage," ASME J. Engineering for Power, 102, pp. 866-874.

[6] Sieverding, C., and Bosche, V. D., 1983, "The use of colored smoke to visualize secondary flows in a turbine-blade cascade," Journal of Fluid Mechanics, Cambridge University Press, 134, pp. 85-89.

[7] Wang, H. P., Olson, S. J., Goldstein, R. J., and Eckert, E. R. G., 1997, "Flow Visualization in a Linear Turbine Cascade of High Performance Turbine Blades," ASME J. Turbomach., 119, pp. 1-8.

[8] Rose, M., 1994, "Non-axisymmetric end-wall profiling in the hpngvs of and axial flow gas turbine," ASME Paper No. 94-GT-249.

[9] Yan, P. J., Gregory-Smith, D. G., and Walker, P. J., 1999, "Secondary Flow Reduction in a Nozzle Guide Vane Cascade by Non-Axisymmetric End-wall Profiling," ASME Paper No. 99-GT-339.

[10] Harvey, N. W., Rose, M. G., Taylor, M. D., Shahpar, S., Hartland, J., and Gregory-Smith, D. G., 2000, "Non axisymmetric Turbine End Wall Design: Part I: Three-Dimensional Linear Design System," ASME J. Turbomach., 122(2), pp. 278-285.

[11] Hartland, J. C., Gregory-Smith, D. G., Harvey, N. W., and Rose, M. G, 2000, "Non axisymmetic Turbine End Wall Design: Part II – Experimental Validation," ASME J. Turbomach., 122(2), pp. 286-293.

[12] Ingram, G., Gregory-Smith, D., Rose, M., Harvey, N., and Brennan, G., 2002, "The Effect of End-wall Profiling on Secondary Flow and Loss Development in a Turbine Cascade," ASME Paper No. GT2002-30339.

[13] Saha, A. K., and Acharya, S., 2006, "Computations of Turbulent Flow and Heat Transfer through a Three Dimensional Non-Axisymmetric Blade Passage," ASME Paper No. GT2006-90390.

[14] Praisner, T. J., Allen-Bradley, E., Grover, E. A., Knezevici, D. C., and Sjolander, S. A, 2007, "Application of Non-Axisymmetric End-wall Contouring to Conventional and High-Lift Turbine Airfoils," ASME Paper No. GT2007-27579.

[15] Brennan, G., Harvey, N. W., Rose, M. G., Fomison, N., and Taylor, M. D., 2001, "Improving The Efficiency of The Trent 500 HP Turbine Using Non-Axisymmetric End Walls: Part 1 Turbine Design," ASME Paper No. 01-GT-444.

[16] Snedden, G., Dunn, D., Ingram, G., and Gregory-Smith, D., 2009, "The Application of Non-Axisymmetric End-wall Contouring in a Single Stage, Rotating Turbine," ASME Paper No. GT2009-59169.

[17] Snedden, G., Dunn, D., Ingram, G., and Gregory-Smith, D., 2010, "The Performance of a Generic NonAxisymmetric End Wall in a Single Stage, Rotating Turbine at On and Off-Design Conditions," ASME Paper No. GT2010-22006.

[18] Schobeiri, M. T., and Lu, K., 2011, "End-wall Contouring Using Continuous Diffusion: A Breakthrough Method and its Application to a Three-Stage High Pressure Turbine," ASME Paper No. GT2011-45931.

[19] Sauer, H., Muller, R., and Vogeler, K., 2001, "Reduction of Secondary Flow Losses in Turbine Cascades by Leading Edge Modifications at the End-wall," ASME J. Turbomach., 123(2), pp. 207-213.

[20] Zess, G. A., and Thole, K. A., 2002, "Computational Design and Experimental Evaluation of Using a Leading Edge Fillet on a Gas Turbine Vane," ASME J. Turbomach., 124(2), pp. 167-175.

[21] Becz, S., Majewski, M. S., and Langston, L. S., 2004, "An Experimental Investigation of Contoured Leading Edges for Secondary Flow Loss Reduction," ASME Paper No. GT2004-53964.

[22] Chung, J. T., Simon, T. W., and Buddhavarapu, J., 1991, "Three-Dimensional Flow near the Blade/End-wall Junction of a Gas Turbine: Application of a Boundary Layer Fence," ASME Paper No. 91-GT-45.

[23] Govardhan, M., Rajender, A., and Umang, J. P., 2006, "Effect of Streamwise Fences on Secondary Flows and Losses in a Two-Dimensional Turbine Rotor Cascade," J. Thermal Sciences, 15(4), pp. 296-305.

[24] Lietmeyer, C., Denkena, B., Krawczyk, T., Kling, R., Overmeyer, L., Wojakowski B., and Seume, J. R., 2013, "Recent advances in manufacturing of riblets on compressor blades and their aerodynamic impact," ASME J. Turbomach., 135(4), pp.1-12.

[25] Denkena, B., Köhler, J., and Wang, B., 2010, "Manufacturing of functional riblet structures by profile grinding," CIRP J. Manufacturing Science and Technology, 3(1), pp. 14-26.

[26] Siegel, F., Klug, U., Kling, R., and Ostendorf, A., 2009, "Extensive Micro-Structuring of Metals using Picosecond Pulses-Ablation Behavior and Industrial Relevance," J. Laser Micro/Nanoeng, 4(2), pp. 104-110.

[27] Pham, D. T., Dimov, S. S., Bigot, S., Ivanov, A., and Popov, K., 2004, "Micro-EDM—recent developments and research issues," J. Materials Processing Technology, 149(1), pp. 50-57.

[28] Weinert, K., Blum, H., Jansen, T., and Rademacher, A., 2007, "Simulation based optimization of the NC-shape grinding process with toroid grinding wheels," Production Engineering, 1(3), pp. 245-252.

[29] Hesselbach, J., Hoffmeister, H. W., and Hlavac, M., 2005, "Micro-grinding–efficient technique for microstructuring hardened steels," Prod Eng, 12(1), pp. 1-4.

[30] Hirt, G., and Thome, M., 2007, "Large area rolling of functional metallic micro structures," Production Engineering," 1(4), pp. 351-356.

[31] Mazumder, J., Schifferer, A., and Choi, J., 1999, "Direct materials deposition: designed macro and microstructure," Material Research Innovations, 3(3), pp. 118-131.

[32] Mazumder, J., Dutta, D., Kikuchi, N., and Ghosh, A., 2000, "Closed loop direct metal deposition: art to part," Optics and Lasers in Engineering, 34(4), pp. 397-414.

[33] Harrison, S., 1989, "Secondary loss generation in a linear cascade of high turning turbine blades," ASME paper No. 89-GT-47.

[34] John, D., and Graham, P., 2012, "A Numerical Investigation into the Sources of End-wall Loss In Axial Flow Turbines," ASME Paper No. GT2012-69173.

[35] Main, A. J., Day, C. R. B., Lock, G. D., and Oldfield, M. L. G., 1996, "Calibration of a four-hole pyramid probe and area traverse measurements in a short-duration transonic turbine cascade tunnel," Experiments in fluids, 21(4), pp. 302–311.

[36] Lee, S. W., Park, S. W., and Lee, J. S., 2001, "Flow characteristics inside circular injection holes normally oriented to a crossflow: Part I: Flow visualizations and flow data in the symmetry plane," ASME J. Turbomach., 123(2), pp. 266-273.

[37] Jeong, J. and Hussain, F., 1995, "On the identification of a vortex," Journal of Fluid Mechanics, vol. 285, pp. 69-94.

[38] Haller, G., 2005, "An objective definition of a vortex," Journal of Fluid Mechanics, vol. 525, pp. 1-26.